Three-Dimensional Structure of the Apo Form of the N-Terminal EGF-like Module of Blood Coagulation Factor X As Determined by NMR Spectroscopy and Simulated Folding[†,‡]

Magnus Ullner,*[,§] Maria Selander,[§] Egon Persson,[∥] Johan Stenflo,[∥] Torbjörn Drakenberg,[§] and Olle Teleman[⊥]

Physical Chemistry 2, Lund University, POB 124, S-221 00 Lund, Sweden, Clinical Chemistry, Lund University, Malmö General Hospital, S-214 01 Malmö, Sweden, and VTT, Biotechnical Laboratory, POB 202, SF-02151 Espoo, Finland

Received November 14, 1991; Revised Manuscript Received April 8, 1992

ABSTRACT: The three-dimensional structure of a 42-residue fragment containing the N-terminal EGF-like module of blood coagulation factor X was determined by means of 2D NMR spectroscopy and computer simulation. The spectroscopic data consisted of 370 NOE distances and 27 dihedral angle constraints. These were used to generate peptide conformations by molecular dynamics simulation. The simulations used a novel functional form for the constraint potentials and were performed with two time steps to ensure rapid execution. Apart from preliminary runs to aid assignment of NOEs, 60 runs resulted in 13 accepted structures, which have two antiparallel β sheets, no α helices, and five tight turns. There is no hydrophobic cluster. The root mean square deviation for the backbone of the 13 conformations is 0.65 ± 0.11 Å against their mean conformation. About half of the side chains have well-defined structure. The overall conformation is similar to that of murine EGF.

A large number of proteins have been found to contain modules homologous to the epidermal growth factor (EGF).[1] Among these proteins are membrane proteins, plasma proteins, and extracellular matrix proteins [for reviews, see Appella et al. (1988), Engel (1989), Carpenter et al. (1990), and Stenflo (1991)]. Some of the proteins contain single EGF-like modules, such as the complement proteins C1r and C1s, whereas other proteins contain multiple modules of this type, often arranged in tandem, e.g., the EGF precursor, thrombomodulin, the transforming growth factor β-binding protein, and the protein encoded by the Notch locus in *Drosophila melanogaster*. The archetype of the EGF-like module, the epidermal growth factor itself, is a 53 amino acid polypeptide with six cysteine residues linked by intrachain disulfide bonds in the typical pattern 1–3, 2–4, and 5–6. Sequence similarity between different EGF-like modules is often limited. Certain EGF-like modules, such as those in thrombomodulin and urokinase, have been demonstrated to participate in protein–protein interactions, but the function of most of these modules is unknown.

All vitamin K-dependent plasma proteins except prothrombin contain EGF-like modules, i.e., factors VII, IX, and X, protein C, and protein Z, which contain two modules each, and protein S, which contains four (Furie & Furie, 1988). The N-terminal modules (except in human factor VII) contain a hydroxylated aspartic acid residue, *erythro*-β-hydroxyaspartic acid (Hya) (Drakenberg et al., 1983; McMullen et al., 1983). In protein S the three C-terminal modules contain *erythro*-β-hydroxyasparagine (Hyn) (Stenflo et al., 1987). The post-ribosomally modified amino acids are formed by enzymatic hydroxylation of aspartic acid and asparagine, respectively. EGF-like modules that contain Hya or Hyn also tend to have two or more negatively charged amino acids N-terminal to the first Cys, i.e., Asp-Gly-Asp-Gln-(Cys)[1] corresponding to residues 46–50 in factor X or Asp-Ile-Asp-Glu-(Cys)[1] in protein S.

Recently, it was demonstrated that the N-terminal EGF-like modules in factor X (Persson et al., 1989), factor IX (Handford et al., 1990), and protein C (Öhlin et al., 1988) each contain one Ca^{2+}-binding site with moderate affinity (K_d = 20–200 μM) whereas the Hya/Hyn-containing EGF-like modules in protein S have very high affinity Ca^{2+}-binding sites ($K_d \approx 10^{-8}$ M; Dahlbäck et al., 1990). These metal ion binding sites must be saturated for the proteins to be biologically active. Calcium binding to EGF-like modules in *Drosophila* Notch (Fehon et al., 1990) seems to be crucial for protein–protein interaction. Sequence similarities suggest that calcium is bound with relatively high affinity to EGF-like modules in several other proteins such as thrombomodulin and the *Drosophila* Notch protein (Dahlbäck et al., 1990; Stenflo, 1991).

Much effort has been put into the determination of solution structures for EGF and the transforming growth factor α (TGF α) by means of 2D NMR techniques. The structures of murine EGF (mEGF) (Montelione et al., 1987, 1992) and human EGF (Cooke et al., 1987) were solved independently, the latter of which is currently being refined (Cooke et al., 1990; Campbell et al., 1990). The three-dimensional structure of TGF α has been studied by several groups (Kohda et al., 1989; Kline et al., 1990; Campbell et al., 1990) and shows extensive similarity to EGF, which is reasonable in view of sequence and functional similarities (Todaro et al., 1980). Neither EGF nor TGF α binds calcium or contains Hya/Hyn.

[†] This work was supported by grants from the Swedish Natural Sciences Research Council, the Swedish Board of Technical Development, and the Swedish Medical Research Council. The NMR spectrometer was purchased with grants from the Knut and Alice Wallenberg Foundation and the Swedish Council for Planning and Coordination of Research.

[‡] We have submitted the coordinates of the accepted conformations to the Brookhaven Protein Data Bank. The simulated folding software is available from the authors.

[§] Physical Chemistry 2.

[∥] Clinical Chemistry.

[⊥] VTT.

[1] Abbreviations: NMR, nuclear magnetic resonance; 2D, two dimensional; NOE, nuclear Overhauser enhancement; NOESY, nuclear Overhauser enhancement spectroscopy; SF, simulated folding; EGF, epidermal growth factor; mEGF, murine EGF; fX-EGF$_N$, residues 45–86 of the light chain in blood coagulation factor X; TGF, transforming growth factor; rms, root mean square; rmsd, root mean square deviation.

0006-2960/92/0431-5974$03.00/0

In order to elucidate structure–function relationships in calcium-binding EGF-like modules in the vitamin K-dependent coagulation factors, we previously made a complete ^{1}H NMR assignment and determined the secondary structure of the calcium-free form of the N-terminal EGF-like module in bovine factor X (fX-EGF$_N$) (Selander et al., 1990). In spite of low sequence identity to EGF, the secondary structure of this module is similar to those of EGF and TGF α, except for the lack of a triple-stranded β sheet linking the N-terminal residues to the major β sheet. Similar results have been obtained for the calcium-free form of human factor IX (Baron et al., 1992).

In this paper we present the three-dimensional structure of the calcium-free form of fX-EGF$_N$ as determined by high-resolution 2D NMR (Wüthrich, 1986; Bax, 1989) and a new simulation approach, which we will refer to as simulated folding (SF). The structure of the calcium-loaded form, where we have located the calcium-binding site, is presented elsewhere (Selander et al., 1992).

Methods

Sample Preparation. The peptide fX-EGF$_N$, containing residues 45–86 from the light chain of the intact protein, was isolated from enzymatic digests of factor X as described previously (Persson et al., 1989). The NMR samples were prepared according to Selander et al. (1990) to a concentration of 3.5 mM and a pH of 5.8. All NMR experiments were performed using the same sample.

NMR Measurements. Two series of NOESY experiments (Bax, 1985) were performed with mixing times of 40, 80, 130, and 200 ms in H_2O and 20, 50, 100, and 200 ms in D_2O. For each series, the 2D NMR experiments were performed one after the other without removing the sample in order to avoid differences in experimental parameters such as shimming, tuning, and water suppression. All spectra were collected on a General Electric Omega 500 spectrometer working at 500.13 MHz. The probe was thermostated to a temperature of 28 °C. A total of 96 scans were acquired per spectrum, and in each 2D experiment 512 spectra with 2048 complex points were collected. The raw data sets were multiplied by a 50° phase-shifted squared sine-bell window function in both dimensions. Zero-filling in the evolution dimension provided final 2D spectra of 1024 × 2048 complex points.

Evaluation of Distance Constraints. In the spectra with the shortest mixing time, i.e., the 40-ms (H_2O) and 20-ms (D_2O) spectra, peak integrals were determined from contours, where each contour represented a power of 2 in intensity. In these spectra, the NOE buildup was assumed to be linear due to the short mixing time (Kline et al., 1988), and thus proton distances were calculated by using the $1/r^6$ distance dependence for the nuclear Overhauser effect in rigid molecules. The distances were calibrated versus distances in known secondary structure (Selander et al., 1990) such as NH–NH and H_α–H_α distances across the β sheet for the H_2O and D_2O spectra, respectively (Williamson et al., 1985). This procedure gave upper bound distance constraints of 2.2, 2.3, 2.5, and 2.8 Å (corresponding to peak heights of 4, 3, 2, and 1 contours) for the 20-ms D_2O spectrum and 2.2, 2.5, 2.8, 3.1, and 3.5 Å (5, 4, 3, 2, and 1 contours) for the 40–ms H_2O spectrum. For spectra with longer mixing time, cross-peaks were categorized solely according to the mixing time at which they first appear, regardless of the actual cross-peak volumes. The constraints were obtained from the assumption of linear buildup for these peaks when appearing, leading to upper bound constraints of 3.9, 4.2, and 4.5 Å for the H_2O spectra and 3.3, 3.7, and 4.5 Å for the D_2O spectra. These distances were found to correlate well with longer known distances in secondary structure elements, for example, with the fact that most NH–NH proton distances in the β sheet were not observed even at 200 ms. All upper bound distance constraints include an error margin of +0.2 Å. For NOEs involving groups not stereospecifically assigned, a further correction was added to the upper limit of the constraint. This correction was 0.9 Å for methylene groups, 1.0 Å for methyl groups, 1.2 Å for intraresidue constraints to aromatic δ or ϵ protons, 2.0 Å for interresidue distances to aromatic δ or ϵ protons, and 2.3 Å for isopropyl groups of valines and leucines. This is similar to the pseudoatom treatment of Kline et al. (1988).

Dihedral Angle Constraints. Constraints for the backbone dihedral angle, Φ, were obtained by measuring the $J_{NH-\alpha}$ coupling constants in a COSY spectrum with a resolution of 1024 × 4096 complex points. $J_{\alpha\beta}$ coupling constants were obtained in a similar manner from a COSY experiment, but using a D_2O solution. For resonances close to the water resonance, coupling constants were estimated from a NOESY spectrum of the same resolution. Two kinds of constraints were obtained: $J_{NH-\alpha} > 8$ Hz corresponds to $-160° < \Phi < -80°$ and $J_{NH-\alpha} < 6$ Hz corresponds to $-80° < \Phi < -40°$, as derived from the Karplus equation. In the latter case, all other possible solutions to the Karplus equation correspond to disallowed regions in the Ramachandran diagram and were ruled out. The method of Wagner et al. (1987) was used to obtain stereospecific assignments and dihedral angle constraints for the side-chain dihedral angle χ^1. Only clear-cut cases can be distinguished in this manner, that is, when one of the $J_{\alpha\beta}$ coupling constants is greater than 10 Hz or both are smaller than 5 Hz.

Computational Procedure. The tertiary structure was generated by means of simulated folding (SF). SF is based on the same principles as restrained molecular dynamics (Kaptein et al., 1985; Clore et al., 1986), but the potential model contains a simplified description of noncovalent interactions. This makes the method similar to dynamical simulated annealing (Nilges et al., 1988a), but the calculation is performed at constant temperature using a different protocol. The Newtonian equation of motion is integrated at 300 K, using a Gear predictor–corrector algorithm with two time steps. A smaller time step of 0.5 fs is used for bond lengths, bond angles, and distance constraints and a longer one, 1.0 fs, is used for dihedral angles, dihedral constraints, and nonbonded repulsions. We note explicitly that as the potential model is a pseudopotential, the time is only pseudotime; likewise the temperature, 300 K, must be regarded as a pseudotemperature. The bounds on interproton distances and dihedral angles derived from the NMR spectra, as well as the bounds on inter-sulfur distances, are referred to as constraints. However, since they are included as terms in the pseudopotential and may be violated, they are not constraints in a mathematical sense.

A common procedure is to generate initial structures with a metric matrix program such as DISGEO (Havel & Wüthrich, 1984, 1985) or DSPACE (Hare et al., 1986; Nerdal et al., 1988) and use restrained molecular dynamics or simulated annealing to optimize these structures (Nerdal et al., 1988; Nilges et al., 1988b; Scheek et al., 1989; Havel, 1991). Our procedure is performed entirely in real space starting from random, extended conformations that subsequently fold under the influence of the pseudopotential (Clore et al., 1986; Nilges et al., 1988a).

The SF procedure was realized as an extended version of the MUMOD program (Teleman & Jönsson, 1987) and executed on an IBM 3090-600 J computer. The procedure will be

described in more detail in a separate communication, including test cases.

Potential Model. The potential terms for the covalent interactions are harmonic in bond lengths and bond angles and periodic for the dihedral angles:

$$U_c = \sum_{\text{bonds}} A_i(r_i - r_{i,e})^2 + \sum_{\text{angles}} B_j(\alpha_j - \alpha_{j,e})^2 + \sum_{\text{dihedrals}} \sum_{n=1}^{3} C_{k,n}(1 - \cos n\varphi_k) \quad (1)$$

where r_i is the actual length of the covalent bond i, $r_{i,e}$ the corresponding equilibrium length, α_j the actual value of the bond angle j, $\alpha_{j,e}$ the corresponding equilibrium value, and φ_k the actual value of the dihedral angle k.

The values of the bond length force constants, A_i, are the same as used previously (Ahlström et al., 1987), but the bond angle force constants, B_j, are set to a uniform, high value of 2000 kJ·mol^{-1}·rad^{-2} to enforce chirality. All dihedral angles are included as in Ahlström et al., but the peptide groups are kept in the trans conformation by setting the constants $C_{k,1}$, $C_{k,2}$, and $C_{k,3}$ for the angles $C_{\alpha,i}$–C_i–N_{i+1}–$C_{\alpha,i+1}$ to 500, 0, and 0 kJ·mol^{-1}, respectively.

The noncovalent interaction is merely a soft repulsion between pairs of atoms:

$$U_{\text{nc},i<j} = \begin{cases} 0, & r_{ij} \geq r_{ij,\min} \\ D(r_{ij,\min}^2 - r_{ij}^2)^2, & r_{ij} < r_{ij,\min} \end{cases} \quad (2)$$

where r_{ij} is the distance between atoms i and j and $r_{ij,\min}$ is chosen so that this potential and the regular Lennard-Jones potential as used by, e.g., MUMOD intersect at 1 kT. The disulfide bridges are handled by means of constraints to which end the $r_{ij,\min}$ for sulfur–sulfur interactions is set to 2.02 Å. D is 1.0 kJ·mol^{-1}·Å^{-4}.

This potential has two major advantages compared to Lennard-Jones and electrostatic terms, which normally form the nonbonded interactions in molecular modeling force fields. First, it saves computer time, partly because the contribution from one pair is somewhat faster to calculate but mainly because the total number of pairs is reduced. The soft repulsion potential is short ranged and is zero outside $r_{ij,\min}$. A spherical cutoff radius, r_{cut}, as short as 4.5 Å can be used, whereas the Coulombic potential is long ranged and requires an r_{cut} of at least 10 Å or approximately 10 times the number of interaction pairs. Second, the energy needed to superpose two atoms is not infinite as in a Lennard-Jones potential; rather it corresponds to about 30 kT depending on $r_{ij,\min}$. This is sufficient to keep atoms apart in regular situations, i.e., where constraints are satisfied, but enables atoms to pass through each other during folding. This possibility reduces the risk of obtaining conformations trapped in knots.

The topology of the distance constraint potential, see Figure 1, is similar to that used by Nilges et al. (1988a), but the functional form is different:

$$U_{\text{dsc},n} = \begin{cases} E_n A \dfrac{(r_n - r_{n,\text{u}})^2}{(r_n - r_{n,\text{u}})^2 + B}, & r_n > r_{n,\text{u}} \\ 0, & r_{n,\text{l}} \leq r_n \leq r_{n,\text{u}} \\ E_n(r_n - r_{n,\text{l}})^4, & r_n < r_{n,\text{l}} \end{cases} \quad (3)$$

where $r_{n,\text{u}}$ and $r_{n,\text{l}}$ are the upper and lower limits of the distance constraint n and r_n is the distance between the atoms of the constraint. A and B are constants, 405 Å^4 and 25 Å^2, respectively. The value of the coefficient, E_n, changes during the simulation (see below). The essential feature of this potential is that since the force is small at large violations of the upper limit, severely violated constraints have less weight than

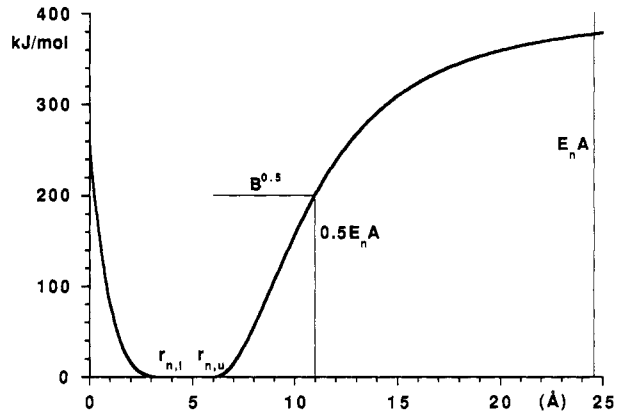

FIGURE 1: Distance constraint potential. $r_{n,\text{l}}$ and $r_{n,\text{u}}$ are the boundaries of the allowed region, in this example 4.0 and 6.0 Å. At large distances U_{dsc} tends toward a plateau value of E_nA. At $r = r_{n,\text{u}} + B^{0.5}$, $U_{\text{dsc},n} = 0.5\ E_nA$. For this example activation would occur at $r = r_{n,\text{u}} + r_{\text{ct}} = 16$ Å.

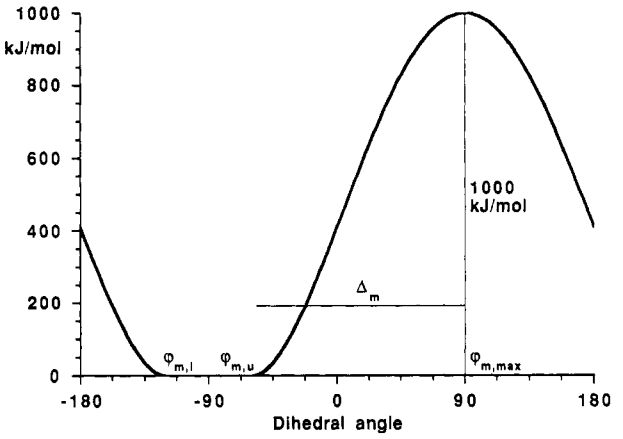

FIGURE 2: Dihedral constraint potential. $\varphi_{m,\text{l}}$ and $\varphi_{m,\text{u}}$ are the boundaries of the allowed region, in this example −60° and −120°. The rotation barrier is always 1.0 MJ/mol.

constraints in the process of being fulfilled.

The lower limit of a distance constraint is 60% of the upper limit without pseudoatom correction. If this limit is smaller than 1.8 Å, the lower limit is set to 1.8 Å. In the case of disulfide bridges, constraints are used for the S–S distances with upper and lower limits of 2.5 and 1.8 Å.

The potential for the dihedral constraints resembles the repulsion potential:

$$U_{\text{dhc},m} = \begin{cases} F_m[(\varphi_m - \varphi_{\text{max},m})^2 - \Delta_m^2]^2, & \varphi_m \text{ outside} \\ 0, & \varphi_m \text{ inside} \end{cases} \quad (4)$$

where φ_m is the value of the dihedral angle of the constraint m, $\varphi_{\text{max},m}$ the angle 180° from the midpoint of the range of angles allowed by the constraint (inside) or, equivalently, the midpoint of the disallowed range (outside), and Δ_m the difference between $\varphi_{\text{max,m}}$ and the upper/lower limit of the constraint; see Figure 2. All these angles are given values in the range [−180°, 180°], and the potential is periodic. F_m has the value $1000/\Delta_m^4$ kJ·mol^{-1}, so that the rotation barrier is 1000 kJ·mol^{-1}.

Protocol. The simulated folding, outlined in Figure 3, is performed in three phases. In phase 1 the distance constraints are treated individually. Initially, all distance constraints are sorted into three classes named active, eligible, and suspended. The distance constraint force (eq 3) is only evaluated for the active constraints. Those constraints are made active, for which the violation $r_n - r_{n,\text{u}}$ is less than a constraint truncation distance r_{ct}, chosen to be 10 Å. A few constraints are set aside

Table I: Initial and Final Constraint Sets[a]

	intraresidual	sequential	medium[b]	long[c]	total	Φ	χ^1
initial set	133	113	32	82	360	15	0
final set	124	119	42	85	370	15	12

[a] The constraints are divided into intraresidual, sequential, medium-range, and long-range constraints. The improvement in between is due to further work with the NMR spectra and to feedback from the calculated structures leading to further assignments. A number of NOEs were discarded because of suspected spin diffusion. [b] Medium range means $1 < |i - j| \leq 5$, where i and j are the residue numbers. [c] Long range means $|i - j| > 5$, where i and j are the residue numbers.

as suspended (see below). Every 40 fs all eligible constraints are checked, and those satisfying the above criterion are made active. Once a constraint is active, it is never deactivated. When a constraint is activated, its coefficient E_n is set to 0.2 kJ·mol^{-1}·Å^{-4} and then increased gradually over 1.0 ps through multiplication by $10^{0.1}$ every 40 fs. The final value is E_n = 63.3 kJ·mol^{-1}·Å^{-4}, and in other words, $E_n \approx 0.2 \times 10^{2.5t}$ kJ·mol^{-1}·Å^{-4}, $0 \leq t \leq 1.0$ ps. In this way constraints for pairs closer in the amino acid sequence are, in a majority of cases, used earlier than constraints for pairs more distant in sequence. This technique of including constraints successively and of increasing coefficients individually, rather than increasing one global coefficient, makes for gentler folding. It is in fact gentle enough to avoid inversions and thus eliminates the need for a chirality potential as sometimes used in simulated annealing work (Nilges et al., 1988a). Their chirality potential is realized as a so-called improper dihedral.

Occasionally, a few eligible constraints will remain inactive, i.e., outside the r_{ct} limit, indefinitely. Therefore, if no constraints have been included during a time period of 1.0 ps, all those eligible constraints are activated whose violations are within 0.5 Å of the smallest violation of an eligible constraint.

Constraints between atoms very close in space but far apart in sequence may, if they happen to be included early in the folding, give rise to tightly folded intermediates that impede rearrangement to account for constraints included later. To circumvent this, constraints with an upper limit of less than 3.0 Å between atoms separated by at least five residues along the chain are put aside in a special group, the suspended group. Only when all other constraints have been activated, i.e., when the eligible group is empty, are all suspended constraints made eligible. Once a constraint has been made eligible, it is never resuspended. In the case of fX-EGF$_N$ seven constraints were suspended [the three disulfide (S–S) constraints, $H_{\beta 2}$ Gln 49 ↔ $H_{\delta 1}$ Tyr 68, H_α Cys 61 ↔ H_α Cys 70, H_α Phe 76 ↔ H_α Ser 84, and $H_{\delta 2}$ Phe 76 ↔ H_α Ser 84]. This exception to the general procedure is added in a somewhat arbitrary manner. It is by no means necessary but, in some runs, leads to better structures with respect to distance constraint energy.

Phase 2 begins 1.0 ps after inclusion of the last distance constraint. During this phase, which lasts 2.4 ps, the force coefficients are simultaneously increased to 470.8 kJ·mol^{-1}·Å^{-4} by multiplication with 1.034 every 40 fs. The value 470.8 kJ·mol^{-1}·Å^{-4} is chosen as large as possible without making the calculation unstable. If the force coefficients are raised much above 500 kJ·mol^{-1}·Å^{-4}, the weight of the other potential terms becomes too small to keep the structure physically meaningful and it starts to fluctuate due to integration inaccuracy. Phase 2 is essentially a brute force minimization of the distance constraint violations, but the success is largely dependent on the result of phase 1. The optimum result of phase 1 seems to be a loosely but on the whole correctly folded structure. Finally, phase 2 is followed by phase 3, during which all force coefficients are kept constant. Phase 3 lasts until the total time is 12 ps. These times are again chosen fairly arbitrarily but are generally more than sufficient to achieve a static conformation.

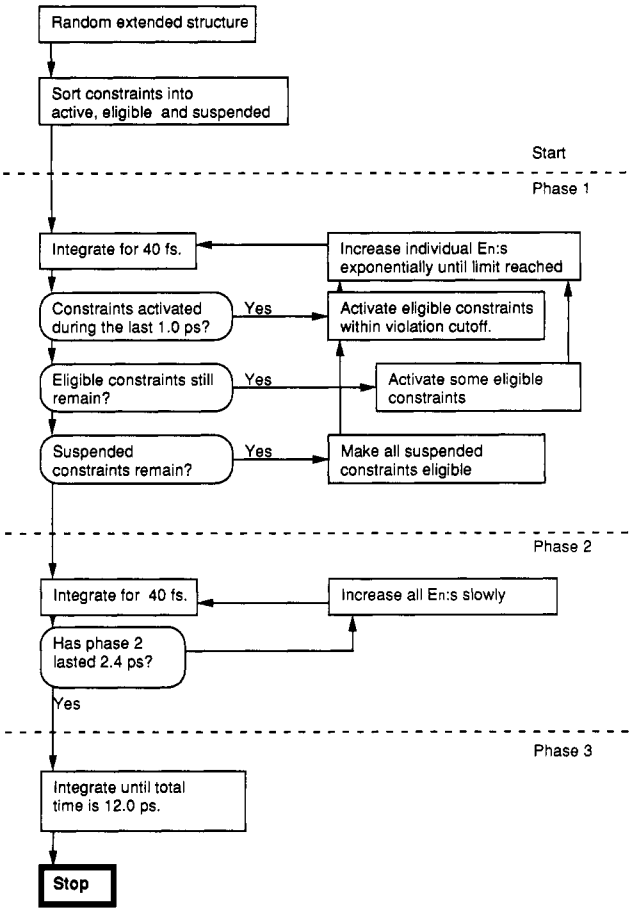

FIGURE 3: Overview of the simulated folding protocol.

For fX-EGF$_N$ a typical run requires about 20 cpu min on an IBM 3090-600 J computer, and thus 60 runs are completed in 20 cpu h.

Initial Conformations. Each SF run was started from a different random conformation. Such conformations were generated by randomizing the Φ and Ψ backbone dihedrals. In order to get slightly extended structures, the Φ and Ψ angles were randomized within ±60° of the β sheet values Φ = −139° and Ψ = 135° or within the dihedral constraints where available. The peptide dihedrals were set trans. All side-chain dihedral angles were completely randomized regardless of any dihedral constraints.

Results and Discussion

The initial set contained 360 constraints. Structural feedback from the first SF runs and continued analysis of spectra resulted in about 20 further constraints. For 14 NOEs which possibly involved more than one proton pair the ambiguities were resolved from preliminary structure calculations as only one candidate was close enough to cause the NOE. About 10 NOEs in the preliminary set were discarded as the intensity was suspected to be affected by spin diffusion. With the three disulfide bridges, the final set of distance constraints amounted to 370 constraints, whereof 85 were long ranged and 42 me-

dium ranged in terms of sequence; see Table I. All cross-peaks in the NOESY spectra were assigned, but 16 NOEs could not be used due to severe overlap. In addition, NOEs were not used when visibly affected by zero quantum contributions. A small number of NH–α and NH–β NOEs were also discarded, for which the upper bound was equal to or longer than the longest distance possible in the bond structure (Wüthrich et al., 1983).

Stereospecific assignments were obtained by NMR methods for β protons in Gln 49, Cys 55, Leu 56, Cys 70, Cys 72, Phe 76, Cys 81, and Phe 83, for δ protons in Asn 57 and Asn 80, and for the ϵ protons of Gln 49. For all other residues, either both $J_{\alpha\beta}$ coupling constants were between 5 and 10 Hz, overlap with other resonances occurred, or the β proton shifts were degenerate. We obtained 15 dihedral angle constraints from the $J_{NH-\alpha}$ coupling constants. Constraints for the χ^1 angle were obtained for Hya 63, Thr 69, Thr 71, and Lys 79.

The first SF runs did not use any stereospecific constraints at all. Either prochiral protons and methyl groups were replaced by pseudoatoms or, if one proton had NOE distances to both members of a prochiral pair, the largest upper limit and the smallest lower limit were used for both constraints. The stereospecific assignments made by NMR were not contradicted by the first SF structures. These assignments were then introduced, thereby removing pseudoatom corrections and extended error margins for all constraints involving the assigned protons. This led to better structural resolution in subsequent structures (Kline et al., 1988). Thereafter, stereospecific assignments, based on the calculations, were made when all converged structures adopted only one conformation for a prochiral proton pair. Such assignments were made only when they were consistent with all distance constraints and coupling constants involving the assigned protons, and a minimum of three converged structures (usually 6–7) was required. By use of a cycle of SF → assignments → SF → etc., stereospecific assignments were obtained for the H_α's in Gly 59, Gly 75, and Gly 78, the H_β's of Glu 51, His 60, Asp 67, Glu 77, Lys 79, and Asn 80, the H_γ's of Ile 65 and of the Leu 56 isopropyl group. The preliminary runs also gave the orientation of all aromatic rings. For 33 out of the 51 distance constraints involving aromatic ring protons of Tyr 68, Phe 76, and Phe 83, it was thus possible to assign the NOEs to a specific side of the corresponding ring using its orientation. This was done when only one of the δ or ϵ protons satisfied a distance constraint (without the pseudoatom correction) and the distance to the other proton was at least 2 Å longer and violated the constraint by more than 1 Å in all converged conformations. This procedure minimizes the use of pseudoatoms which represent the experimental information more crudely. The entire feedback assignment procedure provided tighter constraints for 79 (142 including the stereospecific assignments obtained by NMR) out of the 370 constraints.

The three disulfide bridges merit separate consideration. The first runs did not contain the covalent S_γ–S_γ bonds, nor any constraint representing them. The NOEs were nevertheless sufficient to pair the cysteines correctly. In all later runs, the disulfide bridges were included and only in the form of constraints. No hydrogen bond constraints were used, since hydrogen bonds cannot be determined directly from the NMR spectra.

The structures converge typically within a few picoseconds. Folding pathways vary, but the central β sheet generally forms first. Structures that have not converged are easily recognizable as such from visual inspection and potential energy values. For nonconverged structures the constraint energy is

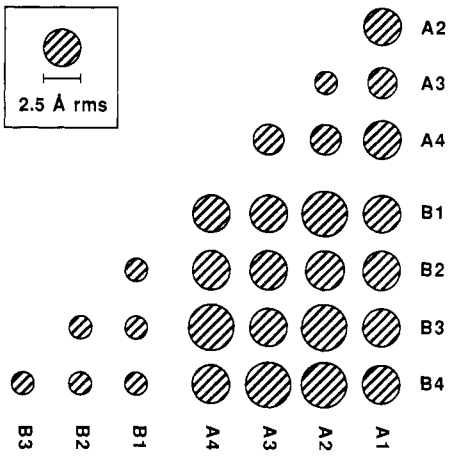

FIGURE 4: Pairwise rms deviations for eight preliminary folding runs, four of which belong to each family with respect to the position of Gln 58. The A1–A4 conformations have the side chain of Gln 58 exposed to the solvent, while in B1–B4 it points into the molecules.

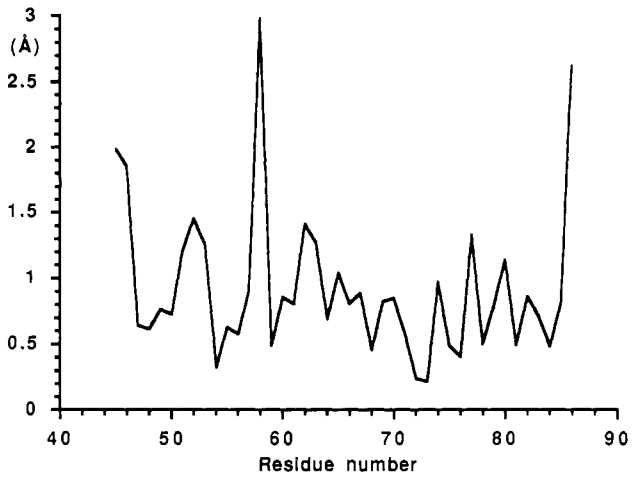

FIGURE 5: Minimum rms deviation for the backbone (N, C_α, and C) for each residue against the peptide mean structure. The value plotted is the minimum of those obtained for the eight structures of Figure 4.

larger than for converged structures, but also the noncovalent repulsion energy is generally larger for nonconverged than for converged structures. Another convenient screening instrument is the sum of all constraint violations. A few converged and nonconverged structures are sufficient to estimate how small this sum has to be in order to indicate convergence.

Though very useful the energy/violation sum screening is not entirely sufficient. Sometimes, locally different conformations satisfy these acceptance criteria equally well. This may represent physically accessible conformations or may be artificial, perhaps due to lack of experimental information. In the few cases where this occurred, the conformations were screened and those were rejected that would entail strong NOEs not present in the spectra.

At one point in the refinement procedure we obtained two structural subfamilies. This could be seen from the superposition of backbone traces, but the following analyses aid the identification of family differences. Figure 4 shows the pairwise rms deviation for eight runs, where four runs belong to each family. Interfamily rmsd's are clearly larger than all intrafamily. Also helpful is Figure 5, which shows the rmsd for each residue against a mean structure but where the rmsd value is the smallest value obtained for any of the eight structures of Figure 4. Peaks in this graph show locations where no individual structure agrees with the mean

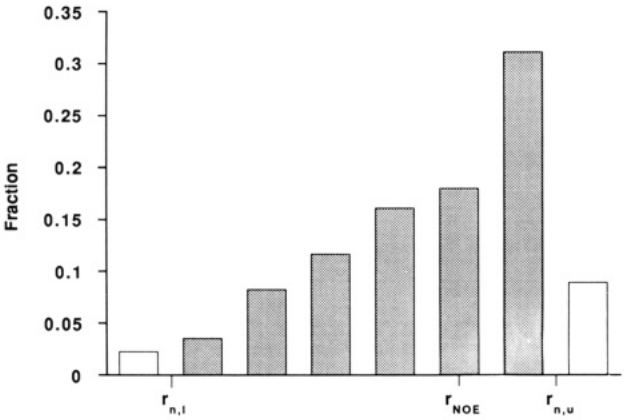

FIGURE 6: Normalized distribution of the constrained distances calculated from the 13 accepted conformations. Satisfied constraints are resolved into six equal regions (filled columns) between each upper and lower limit, $r_{n,u}$ and $r_{n,l}$. r_{NOE} marks the approximate distance corresponding to the NOESY peak intensity for a stereospecific constraint. For a constraint containing a pseudoatom the measured distance lies further to the left. The white columns display the fraction of distances violating upper limits (right) and lower limits (left). The largest violation of an upper limit of a distance constraint is 0.09 Å, and the largest violation of a lower limit is 0.7 Å.

structure—such locations are probably unphysical in the mean structure and are likely points of family difference. The major difference between the two families is that the side chain of Gln 58 points out into solution in one but is situated in the interior of the peptide in the other. The further refinement of the NOE set resolved this ambiguity so that the solvent-exposed position of Gln 58 is the overwhelmingly more likely. The problem with Gln 58 was detected by calculating the NOE resonances a calculated structure would cause, and in this case we found that the buried position of Gln 58 would lead to NOEs not observed in the spectra. This is a primitive so-called back-calculation, which is strictly indispensable for validation of calculated structures.

From the 60 final runs 13 structures with violation sums in the range 0.8–1.6 Å were accepted. The remaining structures had violation sums in the range 1.8–7.2 Å. Figure 6 shows the distribution of the 370 constrained distances within the constraint intervals and the fraction of distances violating upper or lower limits, averaged over the 13 structures. The distribution shows a clustering at the upper limit. This is expected since the error margin of a stereospecific constraint is about 8% of the NOE distance for the upper limit and about 35% for the lower limit. The largest violation, in any of the 13 structures, of an upper limit of a distance constraint is 0.09 Å, and the largest violation of a lower limit is 0.7 Å.

Only a few NOEs connect residues 45–48 and 85–86 with the rest of the molecule. These residues thus show considerable spread in position. In the following the root mean square deviation at optimal rigid body superposition (rmsd) will be based on residues 49–84. The average rms deviation for the 78 pairs that can be combined from the 13 accepted conformations is 0.95 ± 0.18 Å for the backbone atoms (N, C_α, C) and 1.74 ± 0.21 Å for all atoms. When the rmsd is calculated against the mean conformation of the 13, the average rmsd is 0.65 ± 0.11 Å (backbone) and 1.19 ± 0.11 Å (all atoms). Our value of 0.65 Å can be compared to the corresponding rmsd for murine EGF (mEGF), which is 0.81 ± 0.16 Å, indicating that fX-EGF$_N$ and mEGF are equally well-defined structures. The value for mEGF was calculated in our laboratory from the backbone of residues 2–45 for 16 energy-refined conformations provided by Montelione et al. (1992). Figure 7 shows the correlation between number of NOEs per

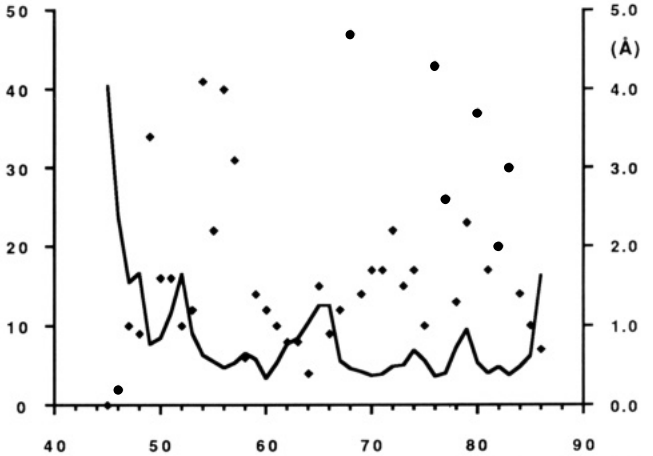

FIGURE 7: Number of NOEs and rms deviation for the backbone (N, C_α, and C) for each residue. The horizontal axis shows the residue number, the left-hand vertical axis the number of NOEs (diamonds), and the right-hand one the rms deviation in angstroms (curve).

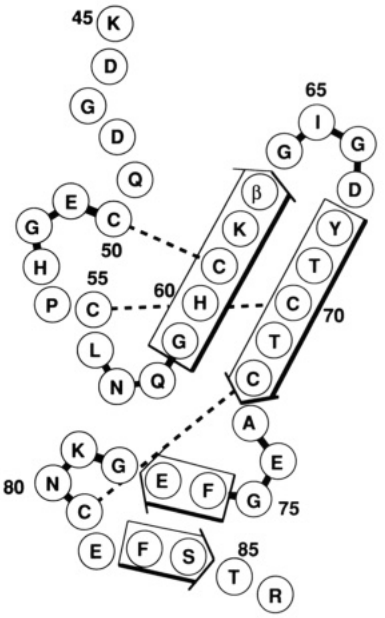

FIGURE 8: Secondary structure of fX-EGF$_N$. Turns are indicated by heavy lines connecting sequential residues. β strands are indicated by arrows and disulfide bridges by dashed lines.

residue and spread in position. We note increased conformational freedom for the N-terminal and to a lesser extent for the C-terminal and the loop 64–67.

Conservation of Backbone Dihedral Angles. The accepted structures extensively agree with respect to backbone Φ and Ψ angles. Terminal residues 45–48 and 85–86 show some spread, probably due to physical mobility (see below). The peptide group between Glu 51 and Gly 52 is rotated in some of the structures. There is also a certain backbone flexibility for residues 65–67 in the turn at the tip of the central β sheet. For these residues, we cannot distinguish whether the spread in conformation is due to multiple physical conformations or merely to insufficient experimental data for identification of the true structure. None of these instances of uncertainty affect the overall conformation.

Structure of fX-EGF$_N$. Figure 8 shows the secondary structure of fX-EGF$_N$, whereas several tertiary representations are given in Figure 9. All elements of secondary structure are generally consistent with our earlier observations (Selander et al., 1990). Residues 59–63 and 68–72 form an antiparallel β sheet with a right-handed twist. The backbone dihedral

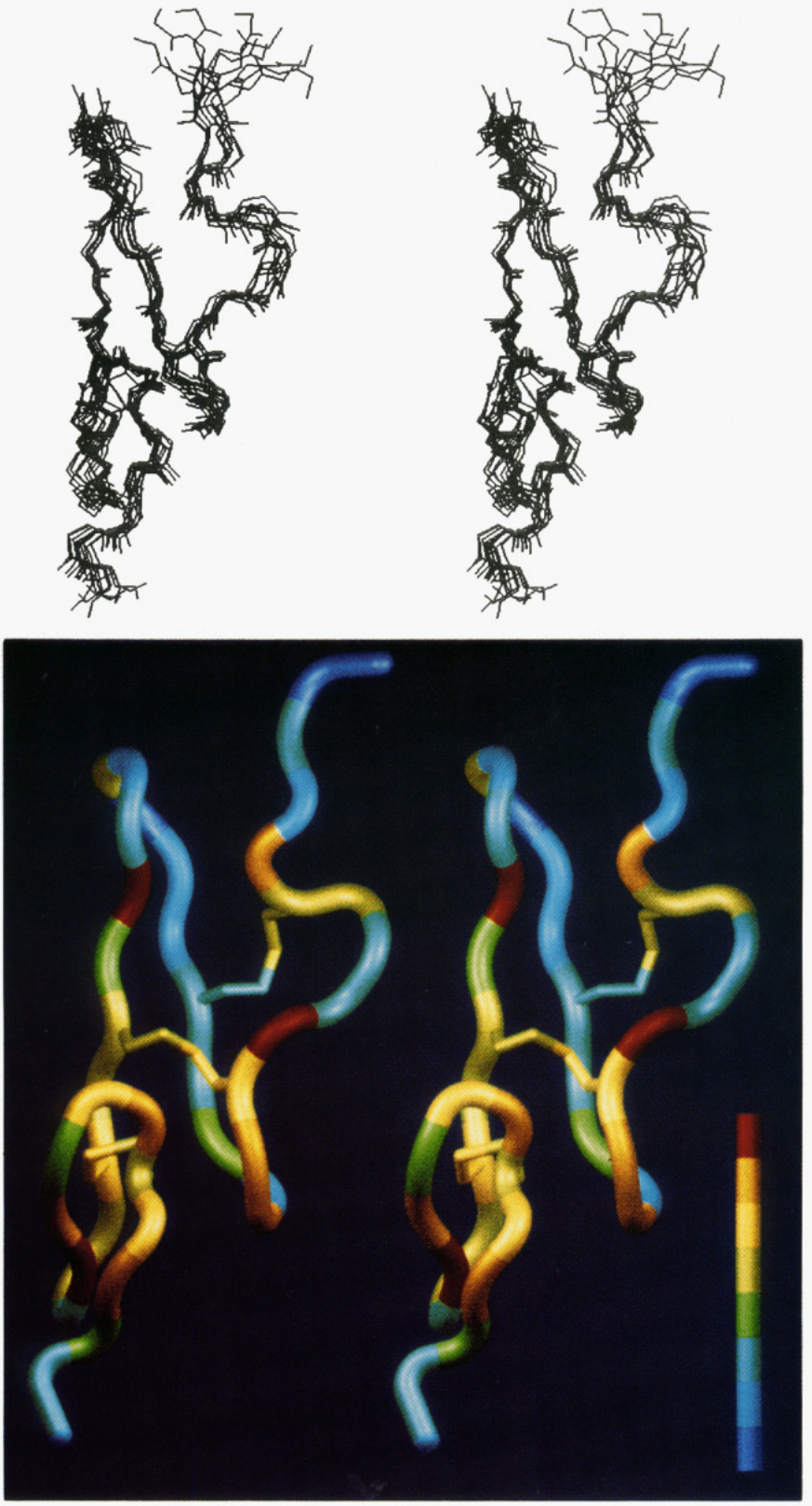

FIGURE 9: (a, top) Stereo backbone traces for the 13 accepted conformations. (b, bottom) Stereoview of the backbone trace based on the α carbon positions. Color coding is according to the number of NOEs involving each residue. The color classes are given in the bar to the right and indicate, from blue to red, 0–4, 5–9, 10–12, 13–14, 15–17, 18–23, 24–40, and 41–∞ NOEs. The picture is realized using the WINSOM software for drawing solid object combined with home-written code and shown on an IBM 5080.

angles are consistent with the type of twisted sheet described by Chothia (1983), but the statistics are not sufficient for positive identification. There is no evidence of N-terminal residues forming a third strand attached to this β sheet as has been observed in murine EGF (Montelione et al., 1987, 1992) and human EGF (Cooke et al., 1987). On the contrary, the position of residues 45–48 is undefined, due to lack of NOEs. We previously observed narrow line widths for these residues and that their amide protons are in fast exchange (Selander et al., 1990). We therefore attribute the conformational spread of the four N-terminal residues to physical mobility.

There are three turns in the N-terminal part of the peptide. Residues 50–53 constitute a type I β turn and residues 56–59 form a type I′ β turn. Residues 64–67 form a tight turn

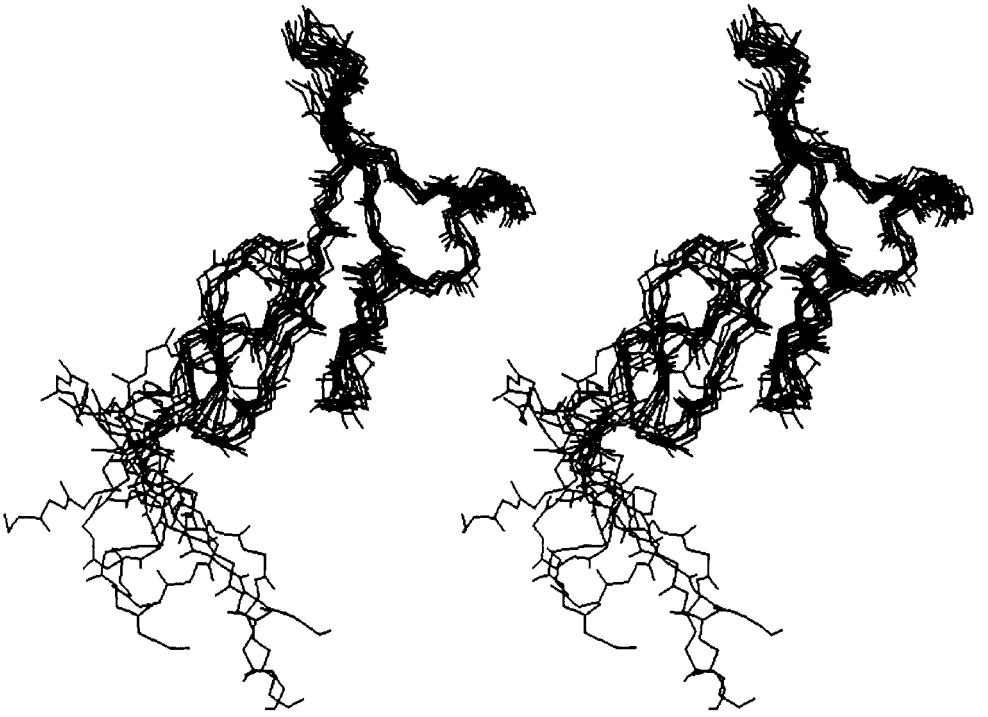

FIGURE 10: Stereo backbone traces for 10 converged and energy-minimized conformations of mEGF provided by Montelione et al. (1992). The triple-stranded β sheet is viewed from the side with the N-terminal strand hidden behind the upper part of the major β sheet.

connecting the two strands of the central β sheet. This turn adopts different conformations and cannot be defined as one of the known types. In some of the SF runs residues 48–51 form a type I β turn. We deem this turn to be an artifact for the following reasons. First, the turn would result in NOEs between H_α Asp 48 ↔ NH Cys 50, H_α Asp 48 ↔ NH Glu 51, H_α Asp 48 ↔ $H_{\beta 1}$ Glu 51, and H_α Asp 48 ↔ $H_{\beta 2}$ Glu 51, NOEs which would fall in uncrowded regions of the spectra but are not observed. Second, it does not appear in all 13 conformations, and third, it is not tight enough to generate the appropriate hydrogen bonds—hydrogen bonds which would be in conflict with the fast exchange of NH in Glu 51.

In the C-terminal part there is an antiparallel β sheet formed by residues 76–77 and 83–84, though the conformation of Ser 84 is rather distorted. Residues 73–76 form a type II β turn and residues 78–81 form a type I β turn. The backbone is kinked at Cys 81 to facilitate the disulfide bridge to Cys 72, and Glu 82 adopts an α-helical conformation, which returns the backbone to the C-terminal β sheet.

In the N-terminal part, human EGF contains three aromatic residues and murine and rat EGF as well as human and rat TGF α contain four, and these peptides feature a mainly aromatic hydrophobic cluster in the N-terminal part. fX-EGF$_N$ contains only one aromatic residue, Tyr 68, in its N-terminal part, and no hydrophobic cluster is observed.

We earlier characterized the contacts between residues 55–56 and 80–82 as a short parallel β sheet. Also, in the simulated structures, a strong hydrogen bond connects NH in Leu 56 with O in Asn 80, as suggested from the secondary structure analysis. However, backbone dihedral angles indicate a β sheet conformation only for Leu 56. The hydrogen bond is rather part of a more complex interregion organization as described below.

Hydrogen Bonds. Table II lists the hydrogen bonds as present in the 13 accepted structures. It is difficult to formulate a criterion for hydrogen bonding as there is no contribution in the pseudopotential that tends to form hydrogen bonds. They are an indirect consequence of the constraint information and may as such deviate locally from ideal hydrogen bond geometry. In a molecular dynamics simulation with full electrostatics, hydrogen bonds would have more strict geometry and could be searched for with stricter criteria. Here, we have chosen to consider as hydrogen bonds the cases where the hydrogen–acceptor distance is less than 3.0 Å and the donor–hydrogen–acceptor angle is greater than 120° in at least 7 of the 13 structures.

Table II: Hydrogen Bonds[a]

acceptor	proton	no. of structures in which present
O Cys 50	NH His 53	7
O Leu 56	NH Gly 59	13
O His 60	NH Thr 71	13
O Lys 62	NH Thr 69	8
O Thr 69	NH Lys 62	13
O Thr 71	NH His 60	13
O Ala 73	NH Phe 76	13
O Glu 77	NH Phe 83	13
O Gly 78	NH Cys 81	11
O Asn 80	NH Leu 56	11
O Phe 83	NH Glu 77	13

[a] The 13 accepted structures were scanned for possible hydrogens, and the table lists those bonds which are present in at least 7 of the 13 structures. The hydrogen bond is considered to exist when the hydrogen–acceptor distance is less than 3.0 Å and the donor–hydrogen–acceptor angle is greater than 120°.

Hydrogen bonds tighten several of the turns. One hydrogen bond connects Cys 50 with His 53 (50–53 = type I β turn), another connects Leu 56 with Gly 59 (56–59 = type I′ β turn), one connects Ala 73 with Phe 76 (73–76 = type II β turn), and finally one connects Cys 81 with Glu 77 (78–81 = type I β turn). The central β sheet is stabilized by hydrogen bonds between His 60 and Thr 71 (two bonds) and between Lys 62 and Thr 69 (also two bonds). The short C-terminal β sheet is stabilized by hydrogen bonds between Glu 77 and Phe 83 (two bonds). One hydrogen bond connects the N-terminal (45–72) and C-terminal (73–86) domains of the molecule, namely, between Leu 56 and Asn 80. All hydrogen atoms involved in these hydrogen bonds exchange slowly. All amide protons reported by Selander et al. (1990) to exchange slowly

or intermediately slowly are involved in hydrogen bonding as listed in Table II, except NH in Gly 64 and Glu 82. Gly 64 is in the beginning of the turn connecting the two strands of the central β sheet, and the amide proton is sterically protected. The NH in Glu 82 is completely covered by the side chains of the 78–81 loop and by the side chains of Leu 56 and Asn 57. This proton is therefore also hidden. Analysis of the accessible surface area using the method of Linse et al. (1990) shows that all amide protons with retarded dynamics are completely hidden from the water.

Organization of Regions. For mEGF and hEGF a subdivision into an N-terminal and a C-terminal subdomain corresponding to residues 45–72 and 73–86 in fX-EGF_N has been proposed (Montelione et al., 1987; Cooke, 1987). In fX-EGF_N several NOEs and a hydrogen bond connect these subdomains. Cys 72, which is just part of the central β sheet, is connected to Ala 73, Phe 76, Glu 77, and Cys 81 by NOEs. Other interregion NOE pairs are Cys 55 ↔ Asn 80, Leu 56 ↔ Asn 80, Leu 56 ↔ Glu 82, Asn 57 ↔ Phe 76, Asn 57 ↔ Glu 82, and Gly 59 ↔ Ala 73. With a distance criterion of 3 Å for considering a residue part of the domain interface, residues 54–59, 68, and 70–72 constitute one side of the contact area, while residues 73, 76, 77, and 79–82 make up the other. Thus, a subdivision into two regions appears unmotivated for fX-EGF_N.

The side chains generally enjoy a certain conformational freedom, and this particularly applies to residues in the termini (45–48 and 85–86). In addition to glycines and cysteines, residues 54–57 have well-defined side chains, as found by visual inspection. Also, most side chains (68–73, 76–78, 80–83) in or close to β strands are well-defined, while Ile 65, in the turn joining the two strands of the central β sheet, features a large conformational spread. Phe 83 is unusual in that its side chain adopts two conformations which are about equally populated.

Comparison to Murine EGF. We have compared the structure of fX-EGF_N to that of mEGF using coordinates made available to us by Montelione et al. (1992). The general organization of mEGF (Figure 10) and fX-EGF_N is similar. The C-terminus of mEGF is longer and more flexible than its counterpart in fX-EGF_N. In fX-EGF_N the first two cysteines are Cys 50 and Cys 55 with but four residues in between. In mEGF this loop contains seven residues and is more flexible. The central β sheet has no third strand in fX-EGF_N. This β sheet has a right-handed twist in both peptides. While it is coiled in mEGF and each of the two strands is one residue longer, it is more or less straight in fX-EGF_N.

ACKNOWLEDGMENTS

We thank G. Montelione and co-workers for generously making available to us the coordinates for mEGF prior to publication. We hereby acknowledge the gift of computer time at Norrdata, Skellefteå. We also thank the Department of Molecular Biophysics for use of graphics equipment and the IBM UK Scientific Centre for the WINSOM software.

Registry No. EGF, 62229-50-9; blood coagulation factor X, 9001-29-0.

REFERENCES

Ahlström, P., Teleman, O., Jösson, B., & Forsén, S. (1987) *J. Am. Chem. Soc. 109*, 1541–1551.

Appella, E., Weber, I. T., & Blasi, F. (1988) *FEBS Lett. 231*, 1–4.

Baron, M., Norman, D. G., Harvey, T. S., Handford, P. A., Mayhew, M., Tse, A. G. D., Brownlee, G. G., & Campbell, I. D. (1992) *Protein Sci. 1*, 81–90.

Bax, A. (1985) *J. Magn. Reson. 65*, 142–145.

Bax, A. (1989) *Annu. Rev. Biochem. 58*, 223–256.

Campbell, I. D., Baron, M., Cooke, R. M., Dudgeon, T. J., Fallon, A., Harvey, T. S., & Tappin, M. J. (1990) *Biochem. Pharmacol. 40*, 35–40.

Carpenter, G., & Wahl, M. I. (1990) *Handb. Exp. Pharmacol. 95*, 69.

Chothia, C. (1983) *J. Mol. Biol. 163*, 107–117.

Clore, G. M., Brünger, A. T., Karplus, M., & Gronenborn, A. M. (1986) *J. Mol. Biol. 191*, 523–551.

Cooke, R. M., Wilkinson, A. J., Baron, M., Pastore, A., Tappin, M. J., Campbell, I. D., Gregory, H., & Sheard, B. (1987) *Nature 327*, 339–341.

Cooke, R. M., Tappin, M. J., Campbell, I. D., Kohda, D., Miyake, T., Fuwa, T., Miyazawa, T., & Inagaki, F. (1990) *Eur. J. Biochem. 193*, 807–815.

Dahlbäck, B., Hildebrand, B., & Linse, S. (1990) *J. Biol. Chem. 265*, 18481–18489.

Davis, C. G. (1990) *New Biol. 5*, 410–419.

Drakenberg, T., Fernlund, P., Roepstorff, P., & Stenflo, J. (1983) *Proc. Natl. Acad. Sci. U.S.A. 80*, 1802–1806.

Engel, J. (1989) *FEBS Lett. 251*, 1–7.

Fehon, R. G., Kooh, P. J., Rebay, I., Regan, C. L., Xu, T., Muskavitch, M. A. T., & Artavanis-Tsakonas, S. (1990) *Cell 61*, 523–534.

Furie, B., & Furie, B. C. (1988) *Cell 53*, 505–518.

Handford, P. A., Baron, M., Mayhew, M., Willis, A., Beesley, T., Brownlee, G. G., & Campbell, I. D. (1990) *EMBO J. 9*, 475–480.

Hare, D., Shapiro, L., & Patel, D. J. (1986) *Biochemistry 25*, 7445-7456.

Havel, T. F. (1991) *Prog. Biophys. Mol. Biol. 56*, 43–78.

Havel, T. F., & Wüthrich, K. (1984) *Bull. Math. Biol. 46*, 673–698.

Havel, T. F., & Wüthrich, K. (1985) *J. Mol. Biol. 182*, 281–294.

Kaptein, R., Zuiderweg, E. R. P., Scheek, R. M., Boelens, R., & van Gunsteren, W. F. (1985) *J. Mol. Biol. 182*, 179–182.

Kidd, S., Kelley, M. R., & Young, M. W. (1986) *Mol. Cell. Biol. 6*, 3094–3108.

Kline, A. D., Braun, W., & Wüthrick, K. (1988) *J. Mol. Biol. 204*, 675–724.

Kline, T. P., Brown, S. C., Jeffs, P. W., Kopple, K. D., & Mueller, L. (1990) *Biochemistry 29*, 7805–7813.

Kohda, D., Shimada, I., Miyake, T., Fuwa, T., & Inagaki, F. (1989) *Biochemistry 28*, 953–958.

Linse, S., Teleman, O., & Drakenberg, T. (1990) *Biochemistry 29*, 5925–5934.

McMullen, B. A., Fujikawa, K., Kisiel, W., Sagasawa, T., Howald, W. N., Kwa, E. Y., & Weinstein, B. (1983) *Biochemistry 22*, 2875–2884.

Montelione, G. T., Wüthrich, K., Nice, E. C., Burgess, A. W., & Scheraga, H. A. (1987) *Proc. Natl. Acad. Sci. U.S.A. 84*, 5226–5230.

Montelione, G. T., Wüthrich, K., Burgess, A. W., Nice, E. C., Wagner, G., Gibson, K. D., & Scheraga, H. A. (1992) *Biochemistry 31*, 236–249.

Nerdal, W., Hare, D. R., & Reid, B. R. (1988) *J. Mol. Biol. 201*, 717–739.

Nilges, M., Gronenborn, A. M., Brünger, A. T., & Clore, G. M. (1988a) *Protein Eng. 2*, 27–38.

Nilges, M., Gronenborn, A. M., & Clore, G. M. (1988b) *FEBS Lett. 229*, 317–324.

Öhlin, A. K., Linse, S., & Stenflo, J. (1988) *J. Biol. Chem. 263*, 7411–7417.

Persson, E., Selander, M., Linse, S., Drakenberg, T., Öhlin, A.-K., & Stenflo, J. (1989) *J. Biol. Chem. 264*, 16897-16904.
Scheek, R. M., van Gunsteren, W. F., & Kaptein, R. (1989) *Methods Enzymol. 177*, 204-218.
Selander, M., Persson, E., Stenflo, J., & Drakenberg, T. (1990) *Biochemistry 29*, 8111-8118.
Selander, M., Ullner, M., Persson, E., Teleman, O., Stenflo, J., & Drakenberg, T. (1992) *J. Biol. Chem.* (in press).
Stenflo, J. (1991) *Blood 78*, 1637-1651.
Stenflo, J., Lundvall, Å., Dahlbäck, B. (1987) *Proc. Natl. Acad. Sci. U.S.A. 84*, 368.
Teleman, O., & Jönsson, B. (1987) *J. Comput. Chem. 6*, 58-66.
Todaro, G. T., Fryling, C. & DeLarco, J. E. (1990) *Proc. Natl. Acad. Sci. U.S.A. 77*, 5258-5262.
Wagner, G., Braun, W., Havel, T. F., Schaumann, T., Go, N., & Wüthrich, K. (1987) *J. Mol. Biol. 196*, 611-639.
Williamsson, M. P., Havel, T. F., & Wüthrich, K. (1985) *J. Mol. Biol. 182*, 295-315.
Wüthrich, K. (1986) *NMR of Proteins and Nucleic Acids*, Wiley, New York.
Wüthrich, K., Billeter, M., & Braun, W. (1983) *J. Mol. Biol. 169*, 949-961.

Surface Binding Kinetics of Prothrombin Fragment 1 on Planar Membranes Measured by Total Internal Reflection Fluorescence Microscopy†

Kenneth H. Pearce, Richard G. Hiskey, and Nancy L. Thompson*
Department of Chemistry, University of North Carolina, Chapel Hill, North Carolina 27599
Received November 13, 1991; Revised Manuscript Received April 14, 1992

ABSTRACT: Total internal reflection fluorescence microscopy (TIRFM) has been employed to investigate the Ca^{2+}-dependent membrane-binding characteristics of fluorescein-labeled bovine prothrombin fragment 1 (F-BF1). Light scattering measurements demonstrated that F-BF1 bound to small unilamellar phosphatidylserine/phosphatidylcholine (25/75, mol/mol) vesicles with an apparent dissociation constant (1.5 ± 0.2 μM) similar to that of unlabeled protein (1.1 ± 0.1 μM). Negatively charged supported planar membranes were constructed by fusing small unilamellar vesicles at quartz surfaces. TIRFM measurements under equilibrium conditions showed that F-BF1 bound to planar membranes with an apparent dissociation constant (0.9 ± 0.2 μM) approximately equal to that on vesicles. Total internal reflection/fluorescence photobleaching recovery (TIR/FPR) curves for F-BF1 on 25 mol % PS planar surfaces were diffusion-influenced at F-BF1 solution concentrations ≤5 μM. Fluorescence recovery rates from samples of high F-BF1 concentrations were slowed by increasing the solution viscosity with glycerol, thus providing further support for a diffusion-limited effect at low F-BF1 concentrations. Analysis of the reaction-limited fluorescence recovery curves at F-BF1 solution concentrations ≥10 μM gave average association and dissociation kinetic rates of $\approx 10^5$ M^{-1} s^{-1} and ≈0.1 s^{-1}, respectively. Kinetic association rates increased significantly with increasing PS, whereas kinetic dissociation rates increased only slightly. Fluorescence recovery curves were nonmonoexponential; possible mechanisms for this behavior are described.

Upon vascular damage, the intrinsic and extrinsic pathways of the blood coagulation cascade converge into a common set of reactions to produce an assembled prothrombinase complex (Jackson & Nemerson, 1980; Mann et al., 1988). A central process in the formation of a fibrin clot is the surface-dependent catalytic conversion of the zymogen, prothrombin, to the active serine protease, thrombin, by prothrombinase (Mann et al., 1990). This enzyme complex is composed of factor X_a, a serine protease, factor V_a, a protein cofactor, and Ca^{2+} assembled on membrane surfaces containing negatively charged phospholipids, such as endothelial cell walls, blood platelets, monocytes, and lymphocytes. Even though thrombin production can occur at slow rates in solution, the localization of prothrombin and the prothrombinase proteins on a membrane surface is required for physiologically relevant activity (Mann et al., 1990). It has been suggested that exposure of negatively charged phospholipids in certain cell types is an event critical in providing a macroscopic surface for the assembly of many blood coagulation proteins. In resting-state platelets, for example, acidic lipids are primarily localized to the inner leaflet. Prothrombin-converting activity by stimulated platelets is greatly enhanced as accompanied by exposure of a procoagulant surface consisting of approximately 25 mol % phosphatidylserine to the membrane exterior (Bevers et al., 1982; Rosing et al., 1985).

To sustain membrane-binding capabilities, several of the factors involved in initiation and regulation of the blood clotting cascade, such as prothrombin, require a vitamin K-dependent posttranslational modification in which glutamic acid is converted to γ-carboxyglutamic acid (Gla). Each of the vitamin K-dependent proteins has a highly homologous amino-terminal domain containing 9–12 γ-carboxyglutamic acid residues (Furie & Furie, 1988). It is presently accepted, in the case of prothrombin, that membrane binding is in part due to electrostatic interactions. One model suggests that Ca^{2+} bridges negatively charged Gla residues to acidic phospholipids, resulting in a reversible, nonpenetrating prothrombin–membrane association. Prothrombin fragment 1, the amino-ter-

† This work was supported by National Science Foundation Grant DCB-8552986 (N.L.T.), a Teacher-Scholar Award from the Camille and Henry Dreyfus Foundation (N.L.T.), and National Institute of Health Grant HL-20161 (R.G.H.).
* To whom correspondence should be addressed.

0006-2960/92/0431-5983$03.00/0